

High Strain-Rate Compression Experiments on Ni/Polyurethane Hybrid Metal Foams Using the Split-Hopkinson Pressure Bar Technique

Markus Felten, Michael Fries, Tomáš Fíla, Petr Zlámal, Jan Falta, Ondřej Jiroušek, and Anne Jung*


Open-cell metal foams are a versatile class of porous lightweight materials, which are predominantly used as kinetic energy absorbers in a wide scope of applications. Based on their bio-inspired inhomogeneous 3D porous structure, they are capable to significantly reduce the mass of structural designs. Starting with a polyurethane (PU) template foam, the specimens in the present contribution are manufactured by an electrochemical nickel (Ni) deposition. This manufacturing process is beneficial regarding both the specimen design and the adjustment of mechanical properties correlated with the Ni-coating thickness. Herein, the strain-rate sensitivity of open-cell Ni/PU hybrid metal foams is investigated by quasistatic compression tests and high-velocity impact tests conducted with a conventional split-Hopkinson pressure bar device.

1. Introduction

Metal foams belong to the class of porous materials. This bio-inspired material class has gained an increasing interest over the last decades as a result of its versatile advantages in the field of lightweight constructions.^[1–3] Metal foams exhibit a high energy absorption capacity under compression, based on a constant stress level over a large strain regime in the stress–strain curve. Hence, cellular materials are predominantly applied as energy absorbers in packaging, automotive, aerospace, and defence industry.^[4]

M. Felten, M. Fries, A. Jung
Applied Mechanics-Foams and Metamaterials
Saarland University
Campus A4.2, Saarbrücken 66123, Germany
E-mail: anne.jung@mx.uni-saarland.de

T. Fíla, P. Zlámal, J. Falta, O. Jiroušek
Faculty of Transportation Sciences
Department of Mechanics and Materials
Czech Technical University in Prague
Konviktská 20, Prague 1 120 00, Czech Republic

 The ORCID identification number(s) for the author(s) of this article can be found under <https://doi.org/10.1002/adem.202100872>.

© 2021 The Authors. Advanced Engineering Materials published by Wiley-VCH GmbH. This is an open access article under the terms of the Creative Commons Attribution-NonCommercial-NoDerivs License, which permits use and distribution in any medium, provided the original work is properly cited, the use is non-commercial and no modifications or adaptations are made.

DOI: 10.1002/adem.202100872

The stress–strain curve under compression loading is divided into three different regions.^[5] The first region outlines an elastic deformation in the majority of the struts, nevertheless yielding occurs in isolated struts. Therefore, this region is referred to as pseudoelastic.^[6] The end of the pseudoelastic region is achieved as soon as the first pore-layer collapses under the so-called plastic-collapse stress (PCS). Starting from this point, a nearly constant stress plateau emerges, where the remaining pore layers gradually collapse. In this damage stage, distinct flow plateaus emerge on the macroscale. The rising stress at the end of the stress plateau is sub-

sequently generated by an increasing contact among the collapsed struts. This area of densification constitutes hereafter the third region of the stress–strain curve.^[2] The particular shape of the stress–strain diagram is moreover based on the specific cellular microstructure of 3D interconnected pores.^[7] Since the foams have to resist multiaxial static as well as dynamic loads during application, an analysis of potential strain-rate effects under compressive loading is essential.^[3,8–11] Strain-rate sensitivity in cellular materials is generally known to be based on four main criteria.^[4] The first criterion affects exclusively closed-cell foams and open-cell fluid-filled foams, where the pore fluid moves slower in comparison to the surrounding framework. As a result, the pressure inside the pore rises and strain-rate effects occurs. The second criterion refers to the pore-framework itself. Calladine and English^[12] observed microinertia effects in cellular materials depending on the particular deformation mode. While the first deformation mode is dominated by bending and shows no strain-rate sensitivity, the second deformation mode is subdivided into two distinct deformation steps, leading to an overall strain-rate sensitivity. The first step involves a plastic compression of the structure followed by a time-delayed rotation at the plastic flow hinges.^[13] Thus, this effect does only depend on the structure of the specimen, however, the third criterion includes furthermore the material properties. According to Gibson and Ashby,^[14] the strain-rate effects of metal foams are correlated with the properties of the strut material itself. The last criterion is based on the shock-wave propagation and enhancement, which occur solely for impact velocities above 50 m s^{-1} .^[15]

Previously, different results on strain-rate effects were observed for the class of open-cell aluminum foams.^[4,16–19]

The PCS shows a clear strain-rate dependency in the majority of this studies.^[4,16–19] However, certain investigations do not show any strain-rate effects for the energy absorption capacity,^[4] while other studies^[17] do show strain-rate effects for this specific benchmark. Nevertheless, a comparison of these results is quite challenging based on different pore geometries, investigated alloys and impact conditions. Therefore, a systematic investigation of strain-rate effects for open-cell metal foams with the same material is required. In recent years, a novel class of open-cell Ni/polyurethane (PU) hybrid foams has been increasingly investigated, as the production process via electrochemical deposition enables the precise adjustment of the mechanical properties.^[9] Felten et al.^[10] studied potential strain-rate effects of open-cell Ni/PU hybrid composite metal foams under low impact velocities up to 550 s^{-1} using a drop tower setup equipped with a high-speed camera and an infrared camera. They observed a constant enhancement of 66% for the density normalized PCS under dynamic impact conditions and associated this strain-rate sensitivity with the microinertia effects described by Calladine and English.^[12] In this context, material-dependent strain-rate effects arising from the nickel coating were excluded, since the energy absorption does not show further significant strain-rate effects. Moreover, the investigation of the evolving specimen temperature revealed a low homologous temperature during the impact, leading to unaffected mechanical properties through thermal softening. Furthermore, it has been demonstrated, that varying the specimen diameter with a constant number of pores in loading direction does not cause size effects.

In this study, similar open-cell Ni/PU hybrid metal foams with two different lengths were manufactured. The strain-rate sensitivity of the Ni/PU hybrid metal foams has been investigated with a conventional split-Hopkinson pressure bar (SHPB) device for strain rates from 10^3 s^{-1} to $5 \times 10^3 \text{ s}^{-1}$. The main objective was to determine the strain-rate sensitivity of the plastic collapse stress as well as the strain-rate sensitivity of the absorbed energy under compressive loading. Both mechanical properties show enhanced values under dynamic loading compared with quasi-static loading as a function of the specimen size. However, the dynamically determined properties outline no further variation and remain constant with increasing strain rates.

2. Experimental Section

2.1. Specimen Preparation

Metal foams were manufactured in a variety of processes, starting from a molten metal, a solid powder, in the state of a vapor or from a metal ion solution.^[20] In the context of this study, the investigated foams, were fabricated by an electrochemical coating process. The framework of Ni/PU hybrid foams comprised an open-cell PU foam (Schaumstoff Direkt Rüdiger Nolte, Enger, Germany) with an average pore size of 20 pores per inch (ppi) and a density of 0.022 g cm^{-3} . The PU template structure was cut in two different sets of specimens. Both sets had a cylindrical shape of 20 mm in diameter but different heights of 10 and 20 mm, respectively. Since PU was not electrically conductive, each specimen had to be coated with a graphite lacquer (CRC Kontakt Chemie, Iffezheim, Germany) to render them

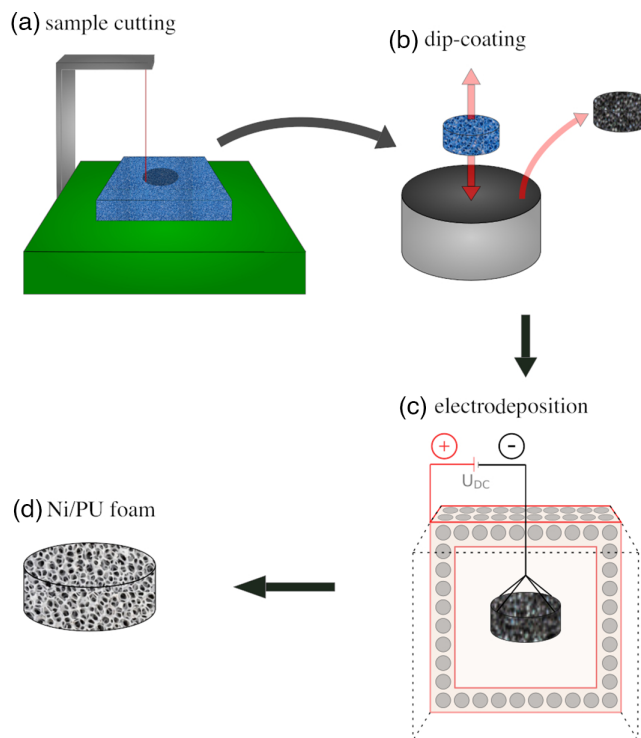


Figure 1. Preparation process: a) cutting of the specimen from PU foam plates by hot-wire cutting, b) dip-coating process, c) electrodeposition inside of a special cathode–anode arrangement, and d) final Ni/PU hybrid metal foam.

electrically conductive. To apply the conductive varnish, the specimens were subjected to the dip coating process shown in **Figure 1b**). During the electrochemical coating process, the carbon-coated C/PU foam cathode was connected to the power supply by a copper wire. Due to the complex and irregular 3D pore geometry, a special cathode–anode arrangement is necessary.^[8] The foam was aligned concentrically inside a hollow double-walled cube as cathode. The sacrificial anode consisting of S-depolarized nickel balls (A.M.P.E.R.E. GmbH, Dietzenbach, Germany) surrounded the cathode on each side of the double-walled cube. Expanded titanium metal serves as a housing for the nickel balls. An overall schematic representation of the preparation process is shown in **Figure 1**. The electrodeposition process was performed with a commercial nickel sulfamate electrolyte containing 110 g L^{-1} nickel (Enthone GmbH, Langenfeld, Germany) at a temperature of $50 \text{ }^\circ\text{C}$, a pH of 3.5, and an average current density of 1.3 mA cm^{-2} . The theoretical coating thickness of both sets of specimens was $150 \text{ }\mu\text{m}$. The mean density and its standard deviation are outlined in **Table 1**.

Table 1. Mean density, quantity, and standard deviation per specimen size.

Height [mm]	Quantity	Density [g cm^{-3}]
10	16	0.796 ± 0.116
20	14	0.926 ± 0.039

2.2. Quasistatic Compression Tests

The quasistatic compression tests were conducted with an Instron 3382 (Instron GmbH, Pfungstadt, Germany) floor model system with a maximum load of 100 kN. All specimens were studied at a strain rate of 0.001 s^{-1} .

2.3. Split-Hopkinson Pressure Bar Principle

The SHPB setup was a classical experimental technique to determine the mechanical properties of various materials at high strain rates.^[8,21–25] The obtained strain rates comprise $10^2\text{--}10^4 \text{ s}^{-1}$. **Figure 2** shows the characteristic schematic setup of the utilized conventional SHPB arrangement. The device consisted of two coaxial rods called incident bar and transmission bar. These bars remained elastic throughout the entire experiment. Strain gauges were mounted equidistantly on both bars. The specimen was located between the two bars and was plastically deformed during the experiment. One end of the incident bar was impacted with a striker bar made of the same material. The resulting compressive pulse propagates through the bar toward the specimen. A strain gauge on the incident bar detected the initial compressive strain pulse ε_I . Since the mechanical impedance of the specimen was lower than the mechanical impedance of the bars, a part of the pulse was reflected as a tensile pulse as soon as the initial pulse reached the specimen. The mechanical impedance was defined as the product of the density of a material and the speed of sound and thus characterized the resistance of a material to the propagation of mechanical oscillations. The reflected pulse ε_R is measured by the strain gauge, as well. The second part of the initial pulse propagated through the specimen and reached the interface between the specimen and the transmission bar. The pulse was reflected as a compressive wave, when it encountered the material of the transmission bar with a higher impedance than the specimen. Therefore, the reflected pulse increased the stress within the specimen. This process continued until the stress reached the yield point and the specimen underwent a plastic deformation. The pulse was furthermore transmitted into the transmission bar and was measured as ε_T by a second strain gauge. **Figure 3** exhibits the characteristic strains measured with the strain gauges occurring during an SHPB experiment. After a specific ramp-in period, the specimen reached the convergence of dynamic forces and underwent a uniform deformation. Taking a 1D wave propagation into account and considering that friction, dispersion, and inertia effects can be neglected leads to the equation

$$\varepsilon_I + \varepsilon_R = \varepsilon_T \quad (1)$$

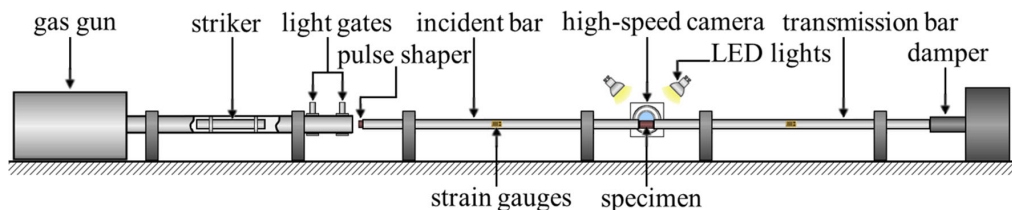


Figure 2. Schematic representation of the experimental SHPB arrangement.

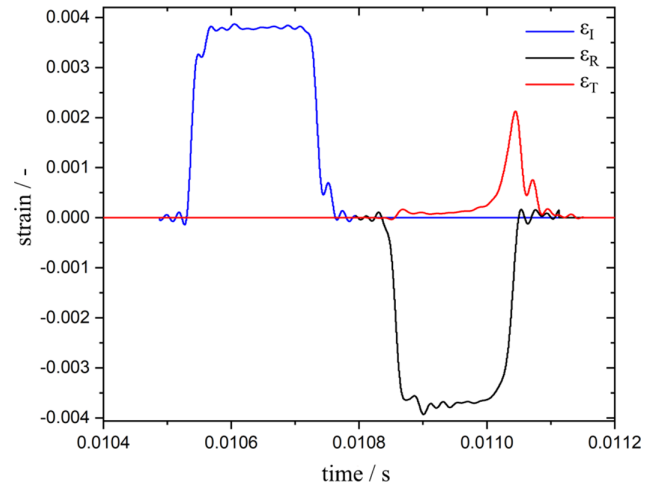


Figure 3. Strains on the incident and transmission bars during an SHPB experiment with a Ni/PU hybrid metal foam specimen: Initial strain ε_I (blue), reflected strain ε_R (black), and transmitted strain ε_T (red).

The nominal strain rate $\dot{\varepsilon}$ is determined with c_b as the wave speed in the bars and l_0 as the initial length of the bars, respectively

$$\dot{\varepsilon}_s(t) = -\frac{2c_b}{l_0} \varepsilon_R(t) \quad (2)$$

The nominal strain ε_s can be calculated by

$$\varepsilon_s = \int_0^t \dot{\varepsilon}_s(t) dt \quad (3)$$

The nominal stress $\sigma_{s,1}$ in the specimen is

$$\sigma_{s,1}(t) = \frac{E_b A_b}{A_s} \varepsilon_T(t) \quad (4)$$

E_b corresponds to the Young's modulus and A_b to the cross-sectional area of the bars. Whereas A_s represents the initial cross-sectional area of the specimen. The calculation of the average stress within the specimen using the transmitted strain ε_T (see Equation (4)) was generally defined as first wave theory. However, if both the incoming and the reflected signals were used to derive the average stress, this is referred to the second wave theory and leads to the expression

$$\sigma_{s,2}(t) = \left(\frac{E_b A_b}{2A_s} \right) (\varepsilon_I(t) + \varepsilon_R(t)) \quad (5)$$

The third wave theory considered the incoming signal $\varepsilon_I(t)$, the reflected signal $\varepsilon_R(t)$, and the transmitted signal $\varepsilon_T(t)$. This leads to the average stress $\sigma_{s,3}$ in the specimen as

$$\sigma_{s,3}(t) = \left(\frac{E_b A_b}{A_s} \right) (\varepsilon_I(t) + \varepsilon_R(t) + \varepsilon_T(t)) \quad (6)$$

The detailed derivation from the 1D wave theory was given in the literature.^[26]

2.4. Instrumentation

All dynamic tests were carried out with an SHPB setup. The incident and transmission bars were made of high-strength aluminum alloy (EN-AW-7075-T6). The bars had a diameter of 20 mm and a length of 1600 mm. The striker had a length of 500 mm and consisted of the identical material with the same diameter as the bars. The striker was accelerated by a custom gas gun with a maximum pressure of 8 bar. The gas gun system consisted of a steel barrel with a length of 2500 mm, a high-flow fast released solenoid valve (366 531, Parker, USA), a 20 L air reservoir equipped with pressure gauge and peripherals. The bars were supported by a set of low-friction polymer liner slide bearings (Drylin FJUM, IGUS, Köln, Germany) mounted in custom-made stainless steel housings. The axes of the bars were exactly aligned to minimize friction and bending of the bars and other undesirable effects. A perfect alignment increases the measurement accuracy. The front faces of the bars were ground precisely to ensure plan-parallelism between the bars. Foil strain gauges (3/120 LY61, HBM, Darmstadt, Germany) with 3 mm active length were attached to the incident bar and the transmission bar to detect the strain wave propagation through the bars. The strain gauges were glued to the bars with a single component low-viscosity cyanoacrylate adhesive (Z70, HBM, Darmstadt, Germany) and cured for 12 h. The measuring points (MPs) were located in the middle of the bars. For amplification of the output signal, the strain gauges were arranged with a Wheatstone half-bridge circuit. The MP signal outputs were amplified using an active differential low noise amplifier (EL-LNA-2, Elsys AG, Niederrohrdorf, Switzerland) with gain of 100, sampled using high-speed 16-bit digitizers (PCI-9826 H, ADLINK Technology Inc., New Taipei City, Taiwan) with a maximal 20 MHz sample rate and triggered by the signal of a through-beam photoelectric sensor (FS/FE 10-RL-PS-E4, Sensopart, Gottenheim, Germany) mounted on the barrel of the SHPB. The specimen deformation was observed using a high-speed camera (FASTCAM SA5, Photron, Tokyo, Japan). A pair of high intensity LED lights (Constellation 60, Veritas, Mountain View, USA) was employed for sufficient illumination. The selected region of interest (ROI) with a pixel resolution of 256×216 provided a frame rate of ≈ 105 kfps. The signal of the through-beam photoelectric sensor was furthermore used to trigger the high-speed camera and for time synchronization of the strain gauge signals with the acquired images. This experimental setup enabled the accurate

evaluation of the micromechanical deformation mechanism of open-cell metal foams during impact. The local principal strain distribution was obtained for different strain conditions with a digital image correlation (DIC) conducted via Istra 4D (Dantec Dynamics, Skovlunde, Denmark).

2.5. SHPB Experiments

The specimens were placed between the incident and the transmission bars after they had been ground on both faces to reduce the distortion of the strain pulse during the transition between the surfaces. The two specimen sets had a diameter of $d_0 = 20$ mm and a length of $l_{01} = 10$ mm and $l_{02} = 20$ mm, respectively. Bertholf and Karnes^[27] recommended a ratio l_0/d_0 of 0.5–1.0 for conventional compression SHPB experiments. This ratio ensured a limited amount of friction and a reasonable uniaxial stress condition. Both ends of the bars were marked with a random black and white speckled pattern to increase the contrast for the subsequent image processing. The gas gun release pressure in a range of 1–8 bar used in the experiments resulted in striker impact velocities ranging from 20 up to 45 m s^{-1} . Copper pulse shapers with diameters ranging from 12 to 18 mm and a thickness of 1.5 mm were placed on the impact face of the incident bar, to reduce the Pochhammer–Chree oscillations, which represent dispersion effects of the elastic wave in the incident bar and make the ramp-in effect at the specimen boundary more significant.^[28,29]

3. Results and Discussion

3.1. Data Processing of SHPB Experiments

Processing the SHPB data is a key task to validate previously defined assumptions. The accuracy of the strain gauges was verified by aligning the incident bar and the transmission bar without a specimen and installing a force sensor at the end of the transmission bar. By manually applied compression, the values of the strain gauges were compared and adjusted with the values of the force sensor (see Figure 4a). The maximum error was 1.6% for the incident bar and 0.7% for the transmission bar. Subsequently, two types of void tests were carried out, the incident bar apart void test and the bars together void test. The incident bar apart void test was performed to analyse the impact velocity, elastic properties of the bar, the wave propagation velocity, damping characteristics, wave shape, strain gauge position error and the linearity of the incident bar. The bars together void test was conducted to analyze the same properties valid for the transmission bar, the quality of the contact between the bars, wave transfer parameters, strain gauge signal equilibrium and friction losses of the system. As longitudinal waves in elastic bars exhibit dispersion, the pulses change as they propagate along the incident and transmission bars. To characterize the wave dispersion effects in the bars, void tests with 500 and 13 mm strikers and no pulse shaper were performed. From the obtained data, the transfer function and the wave propagation coefficient in the frequency domain were calculated, according to the Bacon's method.^[30] The wave transfer function $H^*(\omega)$ of the system was determined from the Fourier transforms of the first

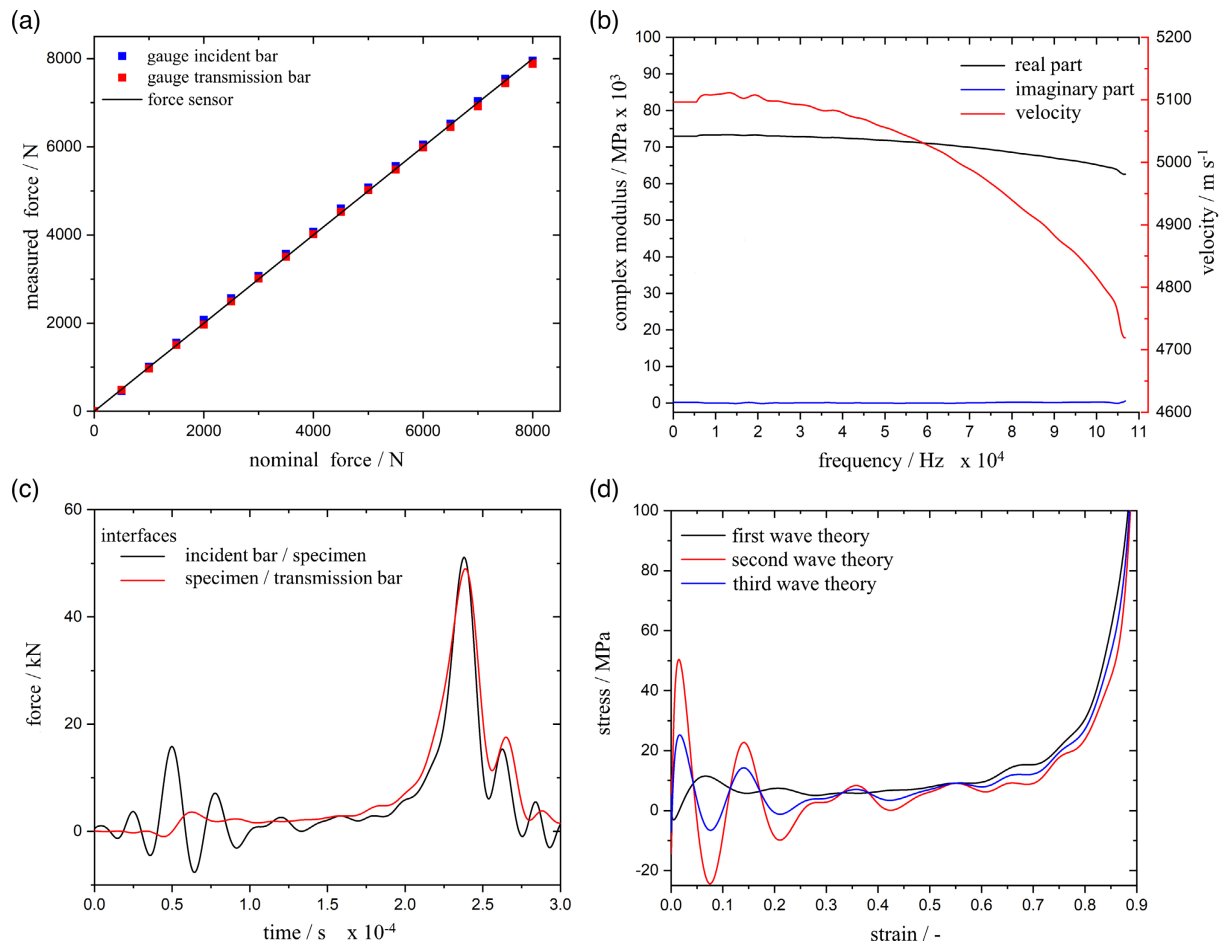


Figure 4. a) Nominal and measured force for the force sensor (black) the strain gauge on the incident bar (blue) and the strain gauge on the transmission bar (red). b) Complex modulus of the bars (left axis) and wave velocity within the bars (right axis) in the frequency domain. c) Measured force after dispersion correction at the interface incident bar/specimen interface (blue) and the interface specimen/transmission bar (red). The force equilibrium is reached in the experiment after 10^{-4} s. d) Stress–strain relation, evaluated with the first (black), the second (red), and the third wave (blue) theory.

measured pulse in the bar $\varepsilon_1(\omega)$ and its reflection $\varepsilon_2(\omega)$ at the free end of the bar. The propagation coefficient $\gamma(\omega)$ was subsequently derived from the equation

$$H^*(\omega) = -\frac{\varepsilon_1(\omega)}{\varepsilon_2(\omega)} = e^{-\gamma(\omega)2d} \quad (7)$$

where d represents the distance between the strain gauge and the free end of the bar. With these calculations, it is feasible to precisely timeshift the strain gauge signals measured in the center of the bars to the specimen boundary. The wave transfer function provides the capability to plot the complex module of the bars and the wave speed in the frequency domain (see Figure 4b)). The real part of the complex module is about 73 GPa and corresponds to the storage module, whereas the imaginary part is close to zero, which indicates almost absolute linear elastic behaviour of the bars. Figure 4c) provides a representative diagram of the force histories during an experiment. For every experiment, the force equilibrium has to be verified, so that Equation (4)–(6) are valid at the same time. The first, the second, and the third wave theories are suitable for the evaluation of the stress–strain

diagram. Figure 4d) shows the stress–strain correlation for the identical experiment evaluated with the three different theories. The three wave theories converge in all the executed experiments. With the acceptable force equilibrium, the first wave theory is usually applied in publications, hence all subsequent calculations are carried out with it. The aforementioned calibrations, pulse shaping techniques, high-speed camera imaging, selected specimen geometries, and dispersion corrections, ensure that the measured response in the SHPB experiment corresponds to the representative constitutive behavior of the specimens.

3.2. Data Analysis of Quasistatic and SHPB Experiments

A sufficient convergence of dynamic forces has been achieved in most of the executed experiments at a displacement of approximately $u = 1$ mm. This corresponds to a total strain of $\varepsilon_1 = 0.1$ for the specimens with an initial length of $l_{01} = 10$ mm and a strain of $\varepsilon_2 = 0.05$ for the specimens with a length of $l_{02} = 20$ mm. **Figure 5** shows a representative stress–strain diagram and the associated force–strain diagram. The dashed line determines

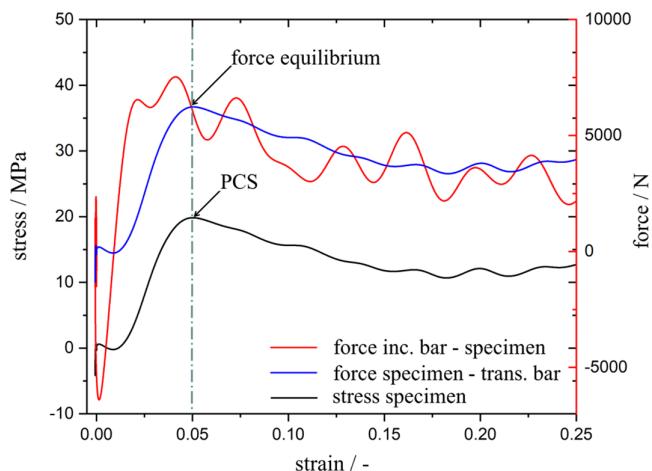


Figure 5. Stress–strain relationship revealed from SHPB experiments on a Ni/PU hybrid metal foam ($l_{02} = 20$ mm) and evaluated with the first wave theory (left axis, black line). Corresponding force of the interface incident bar/specimen (blue line) and the interface specimen/transmission bar force as a function of strain (right axis).

the strain, where the force equilibrium has been reached and when Equation (4) becomes valid. In this case, the force equilibrium occurs simultaneously with the PCS. Therefore, the exact calculation of the stress at the moment of the PCS is only partially possible. However, since the force equilibrium was achieved in most experiments before or closely after the PCS, it is nevertheless included as a true value in the material characterization. A permanent contact between specimen and incident bar is not ensured, between the initial and subsequent impulses. The specimens might slightly change position and the exact calculation of the stress–strain relation is not provided. Therefore, merely the deformation caused by the initial impulse is valid for the calculations. The initial pulse in the experiments executed with the specimens of an initial length $l_{02} = 20$ mm and the lowest impact velocity is insufficient to obtain a complete compression up to the densification point of the foam. Hence, a maximum strain of $\epsilon = 0.3$ is observed under these conditions. **Figure 6** shows a representative stress–strain relation under quasistatic and dynamic

loading. The PCS and the absorbed energy have been selected to initially assess the strain-rate dependency of the Ni/PU hybrid metal foams. The PCS is an essential benchmark as it indicates the transition from a pseudoelastic behavior to a plastic material behavior. A variation of the PCS as function of strain rate would affect the design of a crash absorber. With regard to the primarily application as an energy absorber, the absorbed energy represents a further valuable reference point for the evaluation of the strain-rate dependency. The energy absorption capacity corresponds to the absorbed energy with respect to the specimen volume and is equal to the area under the stress–strain diagram. The energy absorption capacity is calculated up to the maximal mutual strain of $\epsilon = 0.3$, as some specimens were not further compressed within the first impulse. The investigated properties exhibit a large variation, due to a production-related distribution in the specimen density. Therefore, it is necessary to consider the dependency of the specific specimen density on the investigated properties, to exclude influences on a potential strain-rate sensitivity. **Figure 7** shows the PCS and the energy absorption capacity as function of density for the dynamic as well as the quasistatic experiments. Both benchmarks display a linear correlation with density in the investigated range of density. Therefore, hereinafter all values are presented with respect to the individual density. **Figure 8a** shows the PCS normalized to the density as function of strain rate for both specimen sets, after classifying the performed experiments according to the applied strain-rate ranges. Both specimen sets show a distinct variation of the normalized quasistatically determined PCS compared with the PCS under dynamic loading conditions. However, the dynamically determined PCS exhibits no further strain-rate sensitivity with varying strain rates. The specific strain-rate effects acting on the PCS of open-cell Ni/PU hybrid composite metal foams occur merely during the transition from quasistatic loading conditions to dynamic loading conditions and are potentially saturated at moderate loading velocities. Hence, the value of the PCS remains constant with increasing elevated dynamic loading velocities. This effect might arise as a consequence of the microinertia effects described by Calladine and English,^[12] where the second dynamic deformation mechanism of cellular materials leads to a distinct strain-rate sensitivity of the PCS. As the dynamically

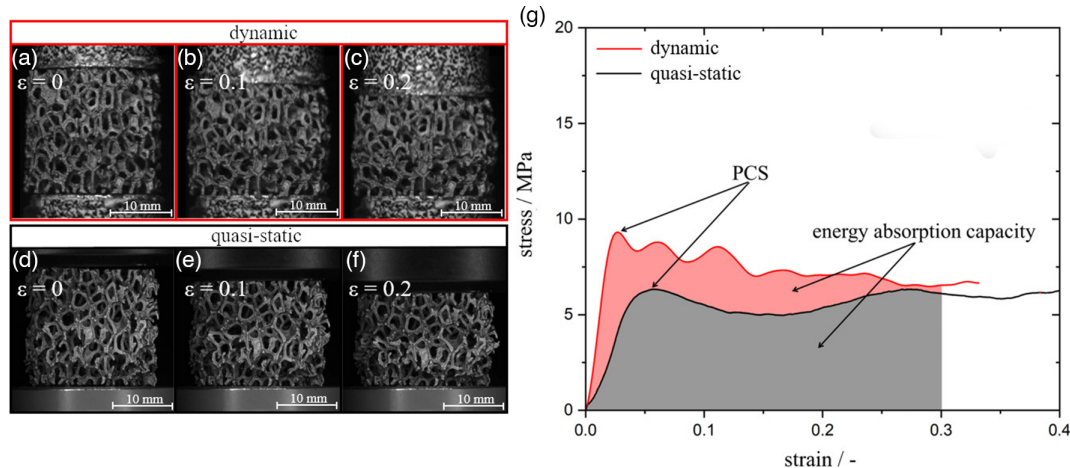


Figure 6. Ni/PU hybrid metal foams under a–c) dynamic and d–f) quasistatic compression loading including (g) a representative stress–strain relation.

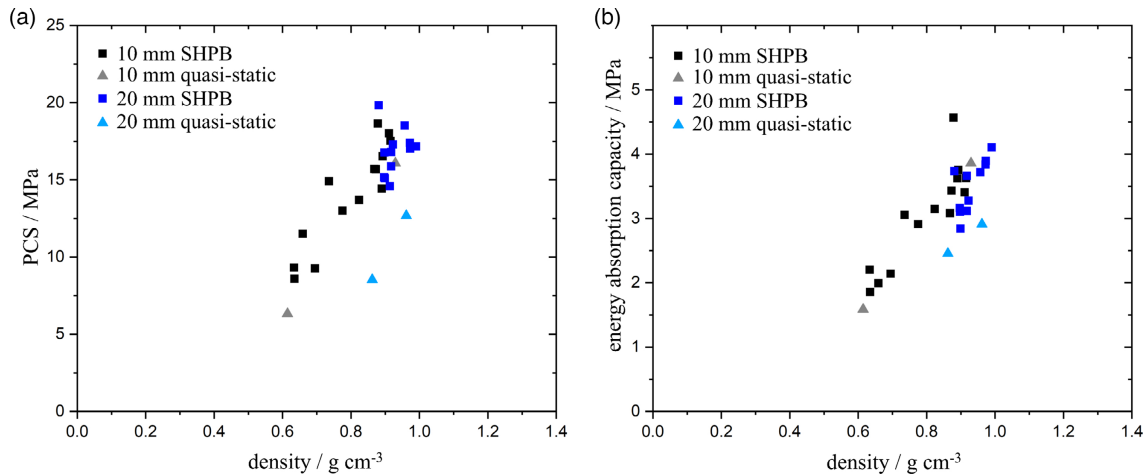


Figure 7. Quasistatically and dynamically determined a) PCS and b) energy absorption capacity as function of the density for specimens with an initial length of $l_{01} = 10$ mm and $l_{02} = 20$ mm, respectively.

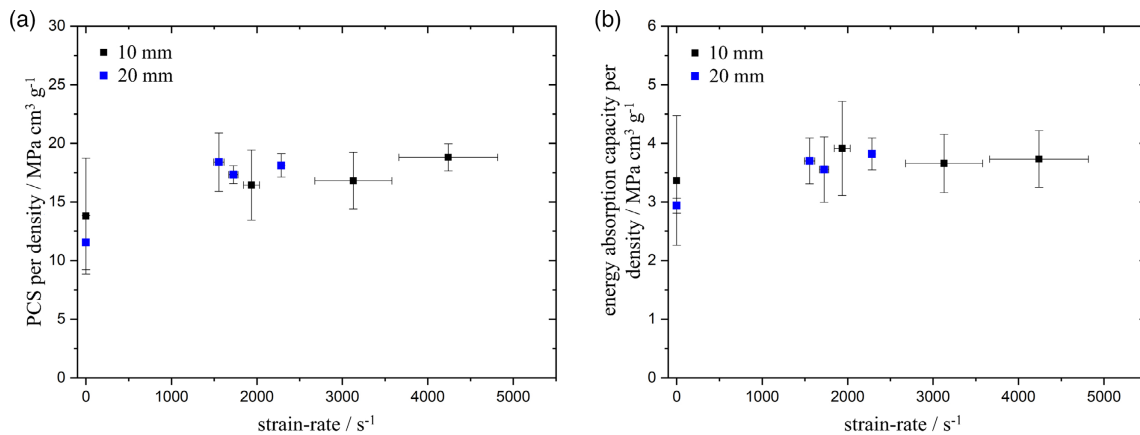


Figure 8. Quasistatically and dynamically determined a) PCS per density and b) energy absorption capacity per density as function of strain-rate for specimens with an initial length of $l_{01} = 10$ mm and $l_{02} = 20$ mm, respectively.

determined normalized PCS shows no further strain-rate sensitivity in the investigated strain-rate range, it is suitable to calculate the mean values to compare them with the quasistatically determined normalized PCS in **Table 2**.

While the strain-rate effect leads to an increase of about 26% for the dynamically determined normalized PCS of the specimen

Table 2. PCS per density and energy absorption capacity per density up to $\varepsilon = 0.3$ for Ni/PU hybrid metal foams investigated under quasi-static conditions and enhanced dynamic impact velocities using SHPB technique.

Length [mm]	Mode	Norm. PCS [MPa cm ³ g ⁻¹]	PCS deviation [%]	Energy abs. cap. [MPa cm ³ g ⁻¹]	Energy deviation [%]
10	qs	13.8 ± 4.9		3.4 ± 1.1	
	dyn	17.4 ± 2.4	26.1	3.8 ± 0.6	12.2
20	qs	11.5 ± 2.3		2.9 ± 0.1	
	dyn	18.1 ± 1.7	57.4	3.7 ± 0.3	26.8

set with an initial length of $l_{01} = 10$ mm, even an increase of about 57% is shown for the specimens set with an initial length of $l_{02} = 20$ mm. This significant size effect may arise as a result of the increased number of pores in the loading direction. A higher amount of pore layers is subjected to microinertia effects, while simultaneously executing micromechanical deformation, which causes an accumulation of the strain-rate effect acting on the PCS. Potential size effects that occur especially during SHPB experiments on small specimens and distort an accurate comparison of the mechanical properties among specimen sets with different initial lengths, are excluded as an explanation for the variation of the dynamically determined normalized PCS.^[31,32] This exclusion is based on the relative calculated strain-rate effects resulting from the comparison of the mechanical property under dynamic loading conditions with respect to the quasistatic loading conditions of the same specimen set.

The obtained results for the normalized PCS are in good agreement with the study of potential strain-rate effects on open-cell Ni/PU hybrid composite metal foams with an initial length of $l = 20$ mm by Felten et al.^[10] conducted at low strain

rates via drop tower experiments. However, the increase in the density normalized PCS for specimens with an initial length of $l_{02} = 20$ mm resulting from the strain-rate sensitivity under dynamic conditions has been found to be 57%, instead of the 66% observed by Felten et al.^[10]. This slightly reduced values of the dynamic PCS in the given investigation may result from the thermal softening of the material. The comparatively higher impact velocities in this study could lead to an increased homologous temperature of the material during the impact and hide the actual strain-rate sensitivity of the material due to thermal softening.^[33] Nevertheless, the observed minor discrepancy could also arise due the material inherent scattering, which equals about 20% independent of the specimen density as well as the applied complex stress state.^[9] Therefore, the conclusion can be drawn, that no additional strain-rate effect occurs by applying moderate strain rates as well as the high strain rates, that affects the normalized PCS of open-cell Ni/PU hybrid metal foams.

Since the material combination of Ni/PU represents a novel class among open-cell foams, the obtained values of the normalized PCS need to be classified within other material combinations of open-cell metal foams. However, a correct comparison of the values is rather challenging, due to varying parameters such as pore size, pore geometry, strain rates, sample size, alloy composition, and density. Therefore, the analysis of the isolated influence of the material is just partially valid. Nevertheless, the normalized PCS of open-cell Ni/PU foams varies in a range of $13\text{--}18 \text{ MPa cm}^3 \text{ g}^{-1}$ and thus exhibits higher values compared with open-cell PU foams and open-cell AlSiMg foams with $0.1\text{--}0.5$, $7.5\text{--}15 \text{ MPa cm}^3 \text{ g}^{-1}$, respectively.^[4,17,19,34,35] However, the PCS is slightly lower compared with open-cell Ni/Al foams, which exhibit a normalized PCS in the range of $22\text{--}25 \text{ MPa cm}^3 \text{ g}^{-1}$.^[4]

In addition to the difficulties described for the PCS, the absorbed energy capacity outlines a further challenge for a valid comparison with other material classes. Usually, higher strains are considered for the calculation of this parameter, than the maximum mutual achieved strain of $\epsilon = 0.3$ in this study. Nevertheless, an energy absorption capacity in the range of $7\text{--}9 \text{ MPa cm}^3 \text{ g}^{-1}$ has been evaluated for the specimen set with an initial length of $l_{01} = 10$ mm up to a strain of $\epsilon = 0.6$, to provide a first comparison of this benchmark with other material classes of open-cell foams. The obtained range for open-cell Ni/PU hybrid metal foam is higher with respect to open-cell AlSiMg foams and lower with respect to open-cell Ni/Al foams with $4\text{--}4.5$ and $20\text{--}22 \text{ MPa cm}^3 \text{ g}^{-1}$, respectively.^[4] For the evaluation of potential strain-rate effects in open-cell Ni/PU foams, the energy absorption capacity up to $\epsilon = 0.3$ was considered, to account for the entire range of specimen geometries and impact velocities. Figure 8b) exhibits the energy absorption capacity with respect to the individual specimen density up to a total strain of $\epsilon = 0.3$ as a function of strain rate. Both specimen sets show a distinct variation of the benchmark determined under quasistatic conditions compared with dynamic loading conditions, as well as an almost constant dynamically determined energy absorption capacity with increasing strain rates. As shown in Table 2, the energy absorption capacity up to a total strain of $\epsilon = 0.3$ rises under dynamic loading condition of about 12% and 27% for the specimen sets l_{01} and l_{02} , respectively. Therefore, this

benchmark exhibits a reduced strain-rate sensitivity relative to the PCS. To determine whether the observed strain-rate effect of the energy absorption capacity results exclusively from the increased normalized PCS or rather from an additional strain-rate effect occurring during sustained compressive strain after the PCS, the averaged normalized stress of the quasistatic and the dynamic experiments as well as the resulting stress enhancement occurring under dynamic loading condition ($\Delta\sigma_{\text{dyn}/\text{qs}}$) with respect to a specific strain after the PCS ($\Delta\epsilon_{\text{PCS}}$) are shown in **Figure 9**. Initially, $\Delta\sigma_{\text{dyn}/\text{qs}}$ decreases up to a strain of $\Delta\epsilon_{\text{PCS}} = 0.2$ after the PCS and reaches a global minimum of almost 0% and 10% for the specimen sets l_{01} and l_{02} , respectively. However, the $\Delta\sigma_{\text{dyn}/\text{qs}}$ increases for both specimen sets with subsequent strain, clearly showing a further strain-rate effect acting under progressive dynamic loading. While the increase in $\Delta\sigma_{\text{dyn}/\text{qs}}$ for the specimen set l_{01} equals merely 10%, a distinct variation of about 40% is shown for the specimens set l_{02} . Based on these results, the strain-rate sensitivity of the normalized energy absorption capacity is not exclusively driven by the strain-rate-sensitive PCS, but rather by a further strain-rate effect occurring with progressive dynamic strain. However, this effect is believed to be activated solely at higher strain rates, since no significant strain-rate effect of the normalized energy absorption capacity occurs under moderate impact velocities.^[10] Furthermore, the second occurring strain-rate effect appears to have a reduced influence on the normalized stress compared with the first one acting on the normalized PCS. To gain a deeper insight into the micromechanical deformation mechanisms during the PCS as well as the second arising strain-rate effect a digital image correlation has been conducted on the dynamically deformed specimens.

3.3. Digital Image Correlation

DIC has been applied in several studies to analyze the micromechanical deformation mechanisms of open-cell metal foams.^[4,10,36] This 2D analysis technique visualizes the local strain distribution on the surface of a specimen under loading conditions and therefore provides a detailed analysis of the micromechanical deformation of open-cell metal foams. **Figure 10** shows the local strain distribution of a specimen with an initial length of $l_{01} = 10$ mm at certain macroscopic strain states after the PCS. Throughout the PCS, a deformation band appears, which undergoes a significant deformation with progressive macroscopic strain. This 2D deformation band represents the pore layer collapsing in the 3D volume of the open-cell metal foam within the second region of the macroscopic stress-strain diagram shown as strain after PCS in **Figure 10g**). In contrast, the remaining areas of the open-cell metal foam exhibit merely a minor local strain distribution, thus primarily the collapsing pore layer contributes to the macroscopic strain. **Figure 11** displays a characteristic DIC evaluation for a specimen from the sample set with an initial length of $l_{02} = 20$ mm. In contrast to the sample set l_{01} , two separate deformation bands appear during the PCS. The first deformation band (dashed blue line) shows a pronounced increasing local strain distribution with progressive macroscopic strain, while the second deformation band (dashed red line) remains in a pre-

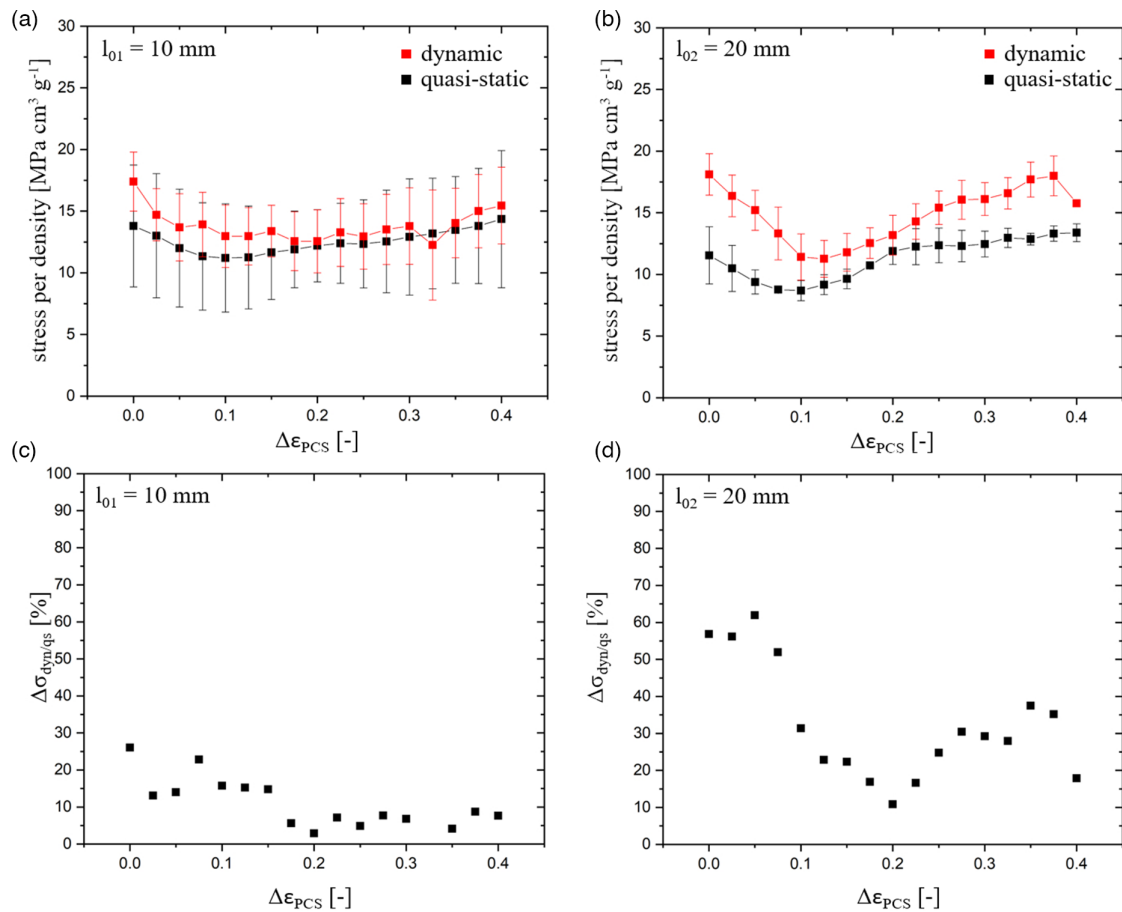


Figure 9. Calculated normalized stress per density of the quasistatic (black) and the dynamic (red) experiments for the specimen sets with an initial length of a) $l_{01} = 10$ mm and b) $l_{02} = 20$ mm as well as the stress enhancement caused by dynamic loading condition ($\Delta\sigma_{dyn/qs}$) (c,d) as function of strain after the PCS ($\Delta\epsilon_{PCS}$).

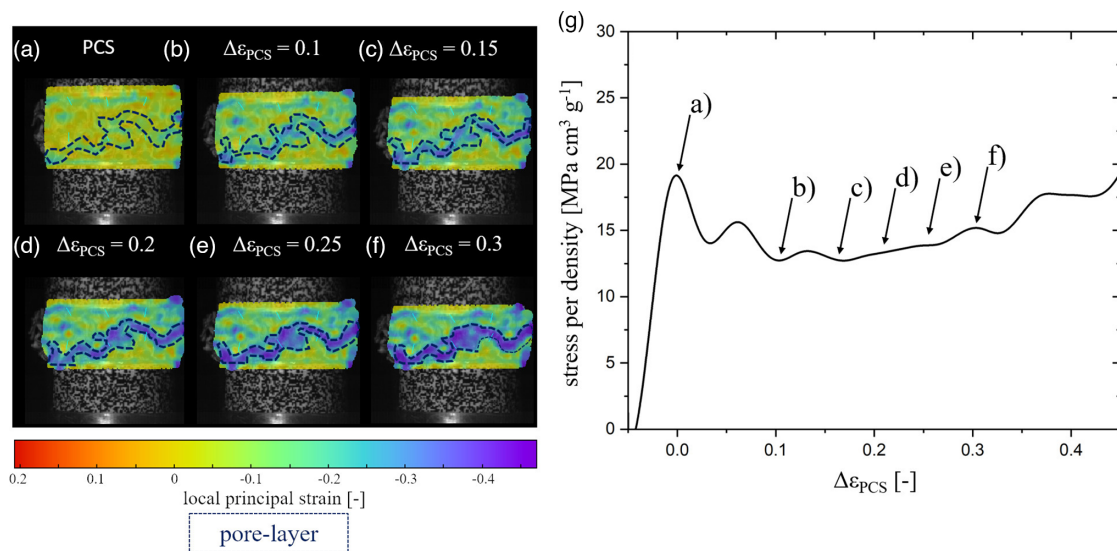


Figure 10. a–f) Local strain distribution at certain strain states after the PCS ($\Delta\epsilon_{PCS}$) as well as the corresponding collapsing pore layer (dashed blue line) evaluated at a sample of the specimen set l_{01} under dynamic loading conditions. g) Corresponding normalized stress per density— $\Delta\epsilon_{PCS}$ diagram.

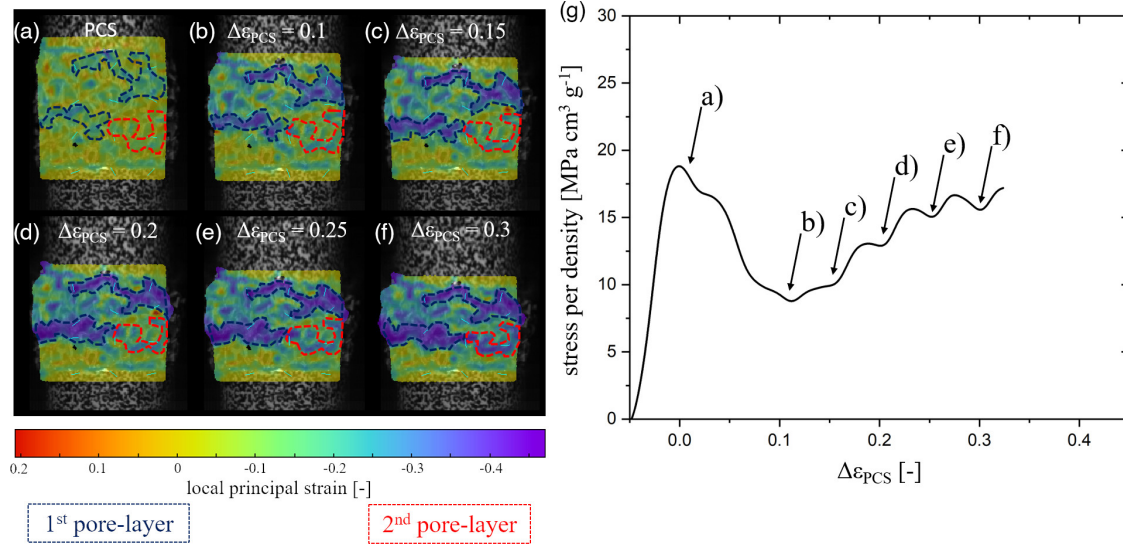


Figure 11. a–f) Local strain distribution at certain strain states after the PCS ($\Delta\epsilon_{PCS}$) as well as the corresponding collapsing first pore layer (dashed blue line) and the second pore layer (dashed red line) evaluated at a sample of the specimen set l_{02} under dynamic loading conditions. g) Corresponding normalized stress per density— $\Delta\epsilon_{PCS}$ diagram.

strained state up to $\Delta\epsilon_{PCS} = 0.2$ and undergoes an increasing local strain distribution at $\Delta\epsilon_{PCS} > 0.2$. Thus, all different pore layers associated with the deformation bands are activated during the PCS, however, exclusively the manufacturing-related weakest pore-layer fails and contributes to the major macroscopic strain up to $\Delta\epsilon_{PCS} = 0.2$. The remaining second pore layer meanwhile remains in a predeformed state and is ultimately subject to further deformation at strain states $\Delta\epsilon_{PCS} > 0.2$, when the first pore-layer has been almost entirely collapsed. The increase in the amount of activated deformation bands during the PCS for l_{02} confirms the previously established assumption, that a higher amount of pore layers in loading direction leads to the observed size effects. The enhanced strain-rate effects occur as a consequence of multiple pore layers, which are simultaneously subjected to a micromechanical deformation, leading to an accumulation of the strain-rate effects acting on the PCS. Since the macroscopic strain for specimen set l_{01} results mainly from the deformation of one pore layer, it also indicates why no further pronounced strain-rate effect has been observed on Figure 9c). In contrast, the second deformation band of l_{02} undergoes a significant deformation at the same strain state ($\Delta\epsilon_{PCS} > 0.2$), where the second strain-rate effect on Figure 9d) occurs. Therefore, the second strain-rate effect occurring in l_{02} at $\Delta\epsilon_{PCS} = 0.2$ most likely arises as a consequence of the deformation of the second pore-layer, which is also affected by microinertia effects. However, the question still remains why the second strain-rate effect at $\Delta\epsilon_{PCS} = 0.2$ is significantly less pronounced compared with the first strain-rate effect acting on the PCS. Based on the previous results, two hypotheses appear reasonable for this effect. The first hypothesis is based on the observed size effects. While for l_{02} two distinct pore-layers are simultaneously subjected to a micromechanical deformation during the PCS resulting in a potentially accumulated strain-rate effects, there is only one pore-layer available for the strain state

$\Delta\epsilon_{PCS} > 0.2$, so that the strain-rate effects have a less pronounced effect on the stress per density under subsequent loading conditions. The second hypothesis, instead, is based on the observed predeformation of the second pore layer. This predeformed pore layer, might rather follow the bending-dominated type 1 deformation mechanism under subsequent dynamic strain, which would also explain the reduced strain-rate sensitivity for the strain states $\Delta\epsilon_{PCS} > 0.2$ in l_{02} . This two novel hypothesis of potentially varying deformation modes during the subsequent dynamic loading of open-cell metal foams are schematically shown in Figure 12. However, which of these two hypotheses finally describe the dominant effect acting on the strain-rate effects under subsequent loading conditions cannot be conclusively determined at the current stage.

4. Conclusion

The mechanical properties under quasistatic and high strain rates up to 5000 s^{-1} of open-cell Ni/PU hybrid metal foams have been experimentally investigated. Quasistatic and SHPB compression experiments were conducted in conjunction with a digital image correlation for a subsequent detailed analysis of the acting micromechanical deformation mechanisms of pore layers under dynamic impact conditions. The experiments have been performed on two specimen sets with different specimen length ($l_{01} = 10 \text{ mm}$, $l_{02} = 20 \text{ mm}$) and thus a varying number of pores in loading direction. The PCS and the energy absorption capacity have been selected to assess the potential strain-rate sensitivity of open-cell Ni/PU hybrid metals foams. The following main conclusions were drawn: 1) The PCS per density exhibits a significant strain-rate sensitivity of 26% and 57% for the specimen sets l_{01} and l_{02} , respectively. The observed size effects might occur as a result of a varying amount of activated pore layers, which are simultaneously subjected to a micromechanical

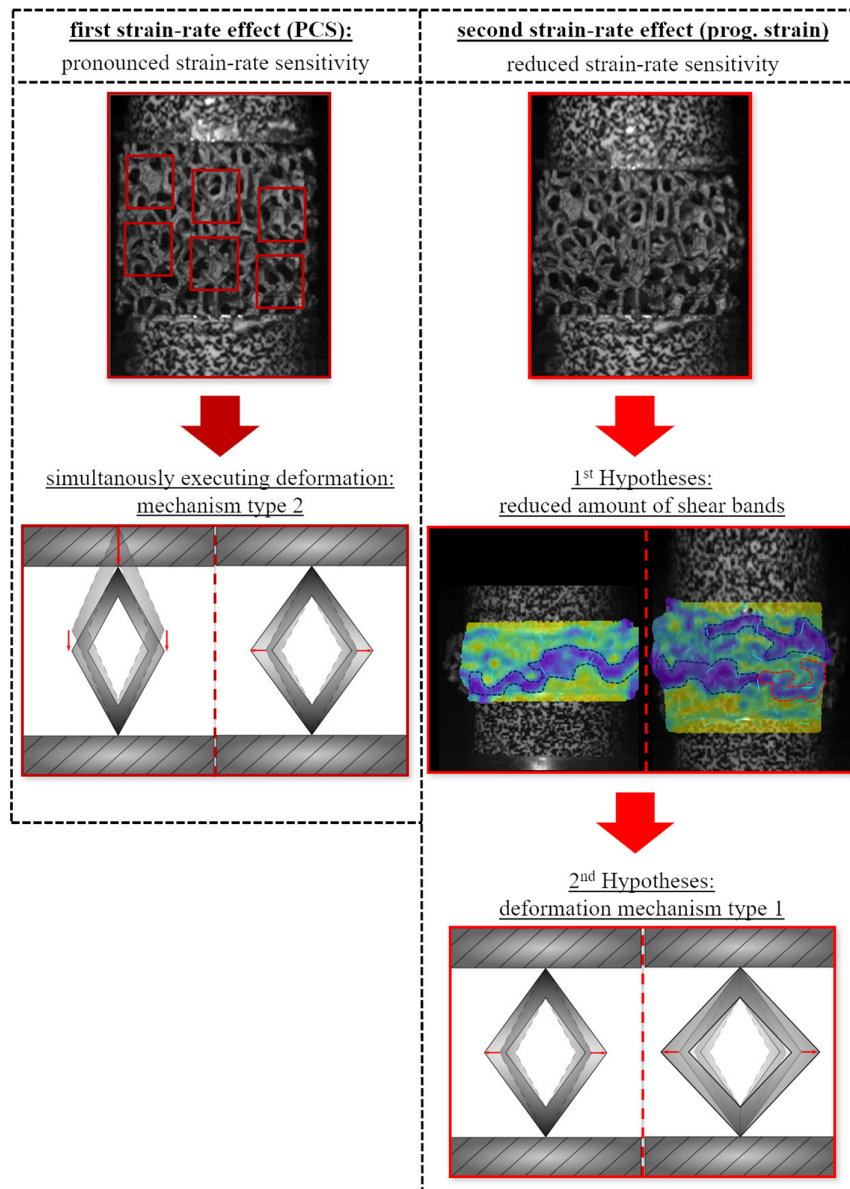


Figure 12. Schematic illustration of the first strain-rate effect acting on the PCS and the second strain-rate effect occurring under dynamic progressive strain with the corresponding two potential deformation mechanisms.

deformation and ultimately causes an accumulated strain-rate effect due to microinertia-related effects; 2) The strain-rate effects show no enhanced influence on the normalized PCS with increasing dynamic strain rates; 3) The investigated energy absorption capacity shows likewise a constant, but reduced strain-rate sensitivity of 12% and 27% for l_{01} and l_{02} , respectively; and 4) For an amount of at least two active deformation bands a second strain-rate effect occurs under progressive dynamic strain ($\Delta\varepsilon_{PCS} > 0.2$). This second strain-rate effect shows a reduced influence on the stress per density, compared with the first strain-rate effect acting on the PCS. Two hypotheses, which are based on different micromechanical models, have been developed to account for this phenomenon. The first hypothesis relies on a reduced number of remaining porelayers under progressive

dynamic strain, similar to the previously described size effects acting on the PCS. The second hypothesis, addresses the pre-formed state of the second porelayer, which could lead to a change in the deformation mechanism and cause a reduced strain-rate sensitivity.

Acknowledgements

The authors acknowledge the financial support from the Operational Programme Research, Development and Education in the project INAFYM (CZ.02.1.01/0.0/0.0/16_019/0000766) and Grant Agency of the Czech Technical University in Prague (grant no. SGS20/141/OHK2/2T/16).

Open access funding enabled and organized by Projekt DEAL.

Conflict of Interest

The authors declare no conflict of interest.

Data Availability Statement

Research data are not shared.

Keywords

composites, digital image correlation, metal foams, split-Hopkinson pressure bar, strain-rate effects

Received: July 10, 2021

Revised: October 26, 2021

Published online: November 11, 2021

-
- [1] M. F. Ashby, R. M. Medalist, *Metall. Trans. A* **1983**, 14, 1755.
- [2] A. Jung, Z. Chen, J. Schmauch, C. Motz, S. Diebels, *Acta Mater.* **2016**, 102, 38.
- [3] J. Banhart, J. Baumeister, A. Melzer, W. Seeliger, M. Weber, *Aluminium-Leichtbau-Strukturen für den Fahrzeugbau*, ATZ-MTZ, Sonderausgabe Wiesbaden, Germany **1998**.
- [4] A. Jung, A. D. Pullen, W. G. Proud, *Composites, Part A* **2016**, 85, 1.
- [5] A. Jung, T. Grammes, S. Diebels, *Arch. Appl. Mech.* **2015**, 85, 1147.
- [6] A. Jung, S. Diebels, *Mater. Des.* **2017**, 131, 252.
- [7] M. F. Ashby, *Metal Foams: A Design Guide*, Butterworth-Heinemann, Boston **2000**.
- [8] A. Jung, E. Lach, S. Diebels, *Int. J. Impact Eng.* **2014**, 64, 30.
- [9] M. Felten, S. Diebels, A. Jung, *Mater. Sci. Eng., A* **2020**, 791, 139762.
- [10] M. Felten, M. Fries, A. Pullen, W. G. Proud, A. Jung, *Adv. Eng. Mater.* **2020**, 22, 1901589.
- [11] J. Šleichrt, T. Fíla, P. Koudelka, M. Adorna, J. Falta, P. Zlámal, J. Glinz, M. Neuhäuserová, T. Doktor, A. Mauko, D. Kytýř, M. Vesenjak, I. Duarte, Z. Ren, O. Jiroušek, *Mater. Sci. Eng., A* **2021**, 800, 140096.
- [12] C. R. Calladine, R. W. English, *Int. J. Mech. Sci.* **1984**, 26, 689.
- [13] X. Y. Su, T. X. Yu, S. R. Reid, *Int. J. Impact Eng.* **1995**, 16, 651.
- [14] L. J. Gibson, M. F. Ashby, *Cellular Solids*, Cambridge University Press, Cambridge New York, USA **1997**.
- [15] V. S. Deshpande, N. A. Fleck, *Int. J. Impact Eng.* **2000**, 24, 277.
- [16] F. Han, H. Cheng, Z. Li, Q. Wang, *Metall. Mater. Trans. A Phys. Metall Mater. Sci.* **2005**, 36, 645.
- [17] F. Yi, Z. Zhu, F. Zu, S. Hu, P. Yi, *Mater. Charact.* **2001**, 47, 417.
- [18] J. L. Yu, J. R. Li, S. S. Hu, *Mech. Mater.* **2006**, 38, 160.
- [19] W. Zhihua, M. Hongwei, Z. Longmao, Y. Guitong, *Scr. Mater.* **2005**, 54, 83.
- [20] J. Banhart, *Prog. Mater. Sci.* **2001**, 46, 559.
- [21] T. Fíla, P. Zlámal, O. Jiroušek, J. Falta, P. Koudelka, D. Kytýř, T. Doktor, J. Valach, *Adv. Eng. Mater.* **2017**, 19, 1700076.
- [22] S. S. Daryadel, P. R. Mantena, K. Kim, D. Stoddard, A. M. Rajendran, *J. Non-Cryst. Solids* **2016**, 432, 432.
- [23] Y. Al-Salloum, T. Almusallam, S. M. Ibrahim, H. Abbas, S. Alsayed, *Cem. Concr. Compos.* **2015**, 55, 34.
- [24] D. M. Williamson *AIP Conf. Proceedings* AIP Publishing, New York, USA **2018**, p. 90015.
- [25] Y. Wei, Z. Lu, K. Hu, X. Li, P. Li, *Ceram. Int.* **2018**, 44, 11702.
- [26] G. T. GRAY III, *ASM Handbook*, ASM international, Ohio, USA Vol. 8 **2000**, p. 462.
- [27] L. D. Bertholf, C. H. Karnes, *J. Mech. Phys. Solids* **1975**, 23, 1.
- [28] W. Chen, B. Song, *Split Hopkinson (Kolsky) Bar*, Springer Science+Business Media LLC Berlin, Germany **2011**.
- [29] B. A. Gama, S. L. Lopatnikov, J. W. Gillespie, *J. Mech. Phys. Solids.* **2004**, 57, 223.
- [30] C. Bacon, *Exp. Mech.* **1998**, 38, 242.
- [31] E. W. Andrews, G. Gioux, P. Onck, L. J. Gibson, *Int. J. Mech. Sci.* **2001**, 43, 701.
- [32] P. Schüler, S. F. Fischer, A. Bührig-Polaczek, C. Fleck, *Mater. Sci. Eng., A* **2013**, 587, 250.
- [33] A. Jung, S. Bronder, S. Diebels, M. Schmidt, S. Seelecke, *Mater. Des.* **2018**, 160, 363.
- [34] T. Allen, J. Shepherd, T. A. M. Hewage, T. Senior, L. Foster, A. Alderson, *Phys. Status Solidi B* **2015**, 252, 1631.
- [35] R. W. Shuttleworth, V. O. Shestopal, P. C. Goss, *J. Appl. Polym. Sci.* **1985**, 30, 333.
- [36] M. Adorna, P. Zlámal, T. Fíla, J. Falta, M. Felten, M. Fries, A. Jung, *Acta Polytech. CTU Proc.* **2018**, 18, 72.